日本磁気学会
ISSN 2432-0250
Journal of the Magnetics Society of Japan
Electronic Journal URL: https://www.jstage.jst.go.jp/browse/msjmag

Vol.41 No.4　2017

Journal

Biomagnetism / Medical Applications

JOURNAL OF THE MAGNETICS SOCIETY OF JAPAN

Vol.41 No.4 2017

日本磁気学会

ISSN 2432-0250

HP: http://www.magnetics.jp/ e-mail: msj@bj.wakwak.com

Electronic Journal: http://www.jstage.jst.go.jp/browse/msjmag

新製品　磁区観察ユニット

既存のプローバ装置で磁区観察を！
小型でシンプル！磁区観察をより手軽に！

※概要・特徴

- プローバ装置などに取り付けることが可能な小型・低価格の磁区観察ユニット
- 面内 / 垂直どちらの磁化方向にも対応
- 社内設計光学系による面内磁区の高コントラスト観察（空間分解能 3μm 以下 ）
- 光学系ヘッドの大きさは、 150×150×300mm 重量も 2kg と軽量・コンパクト
- 白色 LED 光源を用いた高安定性・長寿命
- オプションとして顕微鏡スタンド・ステージ・高機能観察 / 解析ソフトウェアなどを用意

※観察例

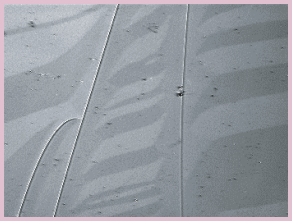

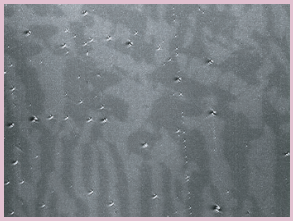

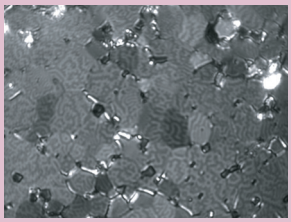

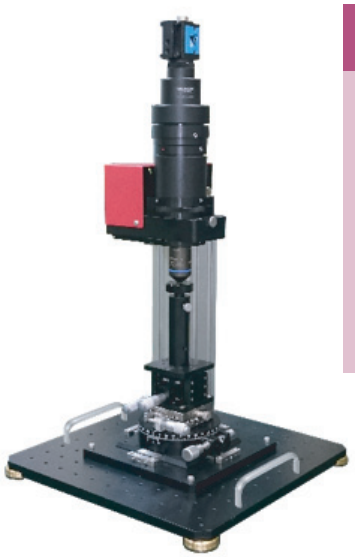

※オプション例

- θ-X-Y-Z 軸ステージ
- 顕微鏡スタンド

※この組み合わせでも重量は約 9kg ですので、 設置場所を選びません

この製品以外に、 30 年の研究現場への対応経験に基づいた高精度・高性能の磁気 Kerr 効果装置、Faraday 装置、 磁区観察顕微鏡など、 各種磁気光学製品の取り揃えがございます。
お気軽にお問合せください。

レーザとレーザ応用システム製品の総合メーカー
NEOARK ネオアーク株式会社
営 業 部／〒156-0041 東京都世田谷区大原2-17-6-108 TEL(03)6379-5539 FAX(03)6379-5688
大阪支店／〒541-0056 大阪市中央区久太郎町2-3-8-201 TEL(06)6271-5123 FAX(06)6271-5110
本社 第1工場・第2工場／八王子市
URL http://www.neoark.co.jp E-mail:info@neoark.co.jp

INDEX

にかほで「みらい」を体験しよう！

アインシュタイン=ド・ハース効果
実験装置を体験

みらい

2035年のみらいを体験

歴史

TDKとエレクトロニクスの歴史を体験

チームラボによるデジタル空間で磁性を体験

TDK Museum

TDK歴史みらい館

http://www.tdk.co.jp/museum/ TDK歴史みらい館

〒018-0402　秋田県にかほ市平沢字画書面15　TEL：0184-35-6580　FAX：0184-35-6853
JR仁賀保駅より 徒歩約10分（タクシーで約3分）

■ 開館時間：10時～18時　　■ 休館日：月曜日（祝日を除く）・当館の定める日
■ 入館料：無料（団体の方は、事前申し込みが必要です）

2016年
10月7日（金）
RENEWAL OPEN!

TDK

世界初！
高温超電導型VSM

新製品

世界初*、高温超電導マグネットをVSMに採用することで
測定速度 当社従来機1/20を実現。
0.5mm cube磁石のBr, HcJ高精度測定が可能と
なりました。
*2014年7月 東英工業調べ

測定結果例

高温超電導VSMによるNdFeB(sint.) 0.5mm cube BHカーブ

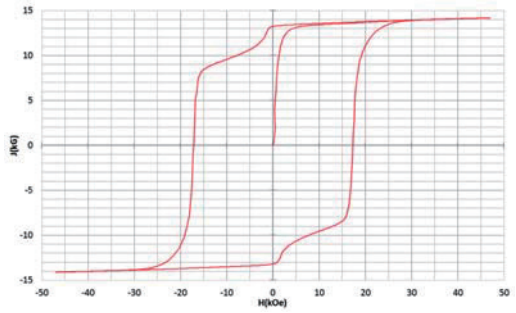

磁化測定レンジ：0.2emu
Br = 13.2kG　　HcJ = 17.2kOe

高温超電導VSMによるNdFeB(sint.) 1mm cube BHカーブ

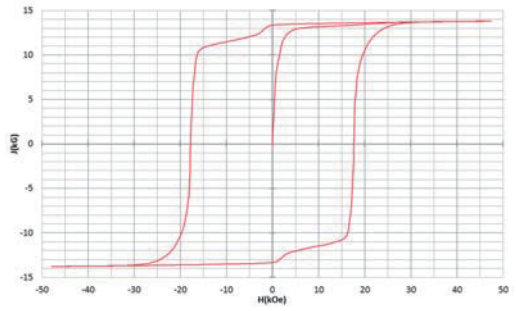

磁化測定レンジ：2emu
Br = 13.3kG　　HcJ = 17.7kOe

高温超電導VSMによるNdFeB(sint.) 4mm cube BHカーブ

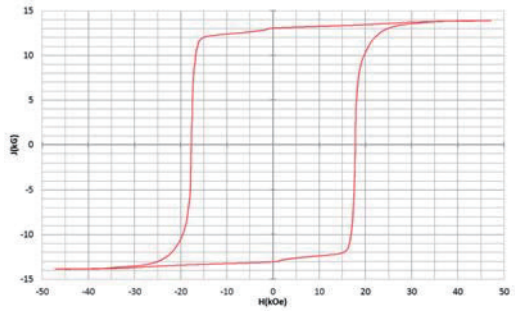

磁化測定レンジ：100emu
Br = 13.1kG　　HcJ = 17.8kOe

高速測定を実現

高温超電導マグネット採用により、高速測定を実現しました。Hmax= 5Tesla, Full Loop 測定が2分で可能です。
（当社従来機：Full Loop測定　40分）

小試料のBr,HcJ高精度測定

0.5mm cube 磁石のBr,HcJ 高精度測定ができ、表面改質領域を切り出しBr,HcJの強度分布等、微小変化量の比較測定が可能です。
また、試料の加工劣化の比較測定が可能です。

試料温度可変測定

−50℃～+200℃温度可変UNIT（オプション）

磁界発生部の小型化

マグネットシステム部寸法：0.8m×0.3m×0.3m

TOEI 東英工業株式会社
http://www.toeikogyo.co.jp
〒194-0035 東京都町田市忠生1-8-13
TEL：042-791-1211 FAX：042-792-0490
E-mail : sales@toeikogyo.co.jp

有限要素法解析ソフトウェア COMSOL Multiphysics®

COMSOL MULTIPHYSICS®

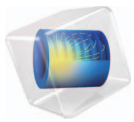

マルチフィジックスの進化論

無制限・強連成で実現象に即したシミュレーション事例のご紹介

永久磁石を利用した磁気軸受の解析例

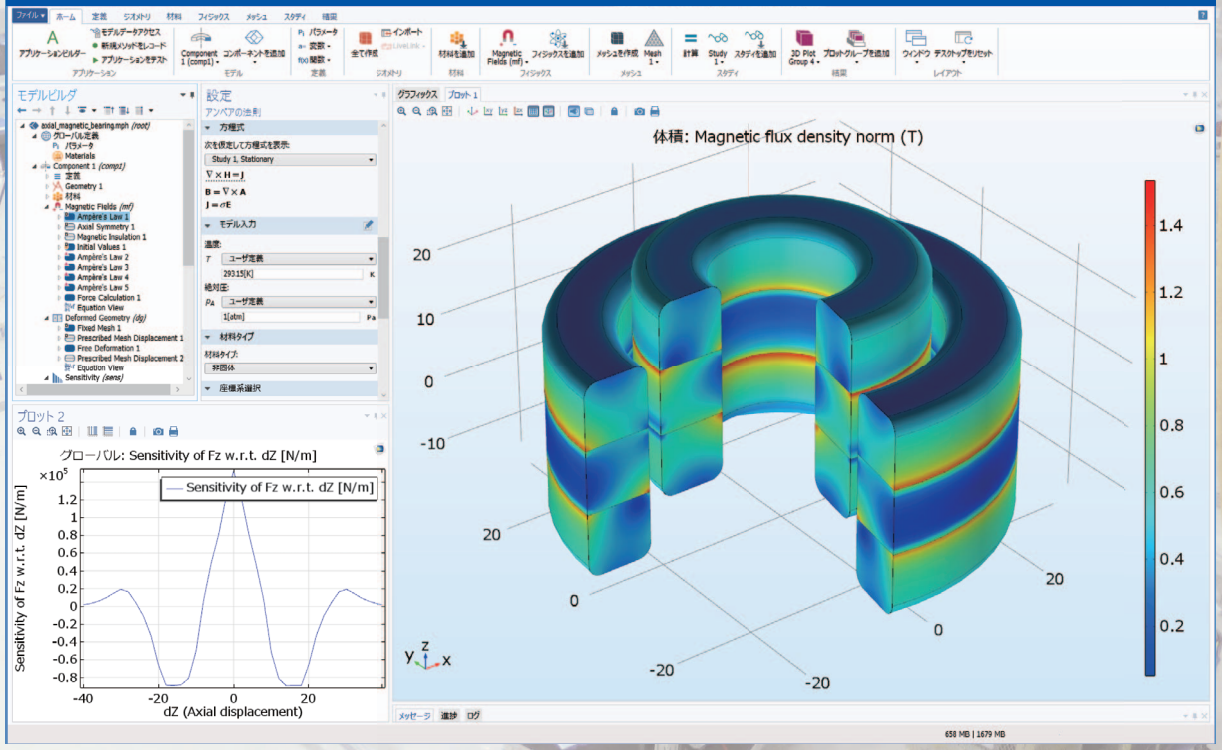

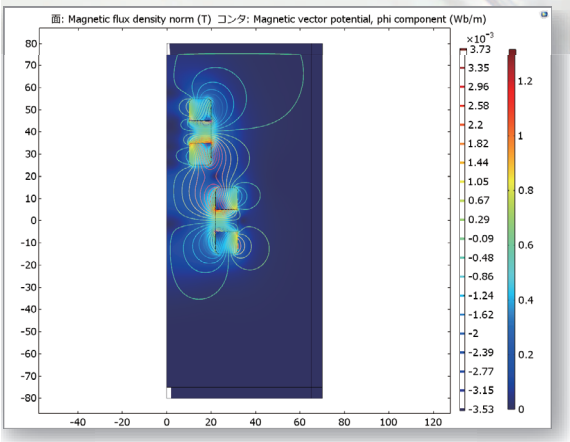

永久磁石を使用した磁気軸受

永久磁石を使用した軸受はターボ機械、ポンプ、モータ、発電機やフライホイール式エネルギー貯蔵システムなど、様々な分野で使用されています。非接触かつ潤滑不要で保守整備を大幅に省略できる点は、従来の機械式ベアリングと比べて重要なメリットです。
この例では、軸方向の永久磁石軸受の磁気力と剛性などの設計パラメータを計算する方法を示しています。

※AC/DCモジュールはCOMSOL Multiphysicsと併用するアドオン製品です。

AC/DC モジュールの適用例

- AC/DC 電流分布、電場分布
- バイオヒーティング
- コイルとソレノイド
- SPICE 回路とフィールドシミュレーション
- 接触抵抗
- 電磁両立性 (EMC) および電磁妨害 (EMI)
- 電磁力およびトルク
- 電磁力シールド
- 電気機械の変形
- ホール効果を利用したセンサ
- インシュレータ、コンデンサ、誘電体
- モータ、ジェネレータ、および他の電気機械
- 非線形材料
- 寄生容量とインダクタンス
- 永久磁石と電磁石
- 多孔質材料
- 抵抗および誘導加熱
- センサ
- 超伝導体
- 変圧器とインダクタ

COMSOL Multiphysics® なら、今まで不可能だった 3 種以上のマルチフィジックス解析を強連成で実現できます。30 日間全機能無料トライアル、無料の導入セミナー、1000種を超える世界の様々な事例をご提供いたします。詳しくは、下記の弊社営業部までお問い合せください。

COMSOL

http://www.comsol.jp

KESCO KEISOKU ENGINEERING SYSTEM
計測エンジニアリングシステム株式会社
http://www.kesco.co.jp/comsol/
Tel : 03-5282-7040 ・ Fax : 03-5282-0808

Journal of the Magnetics Society of Japan
Vol. 41, No. 4

Electronic Journal URL: https://www.jstage.jst.go.jp/browse/msjmag

CONTENTS

J. Magn. Soc. Jpn., **41**, 70-74 (2017)

<Paper>

Evaluation Method of Magnetic Sensors Using the Calibrated Phantom for Magnetoencephalography

D. Oyama, Y. Adachi, and G. Uehara

Applied Electronics Laboratory, Kanazawa Institute of Technology, *Amaike 3, Kanazawa, Ishikawa 920-1331, Japan*

In recent years, many kinds of magnetic sensors have been developed for biomagnetic measurement, such as magnetocardiography (MCG) and magnetoencephalography (MEG). However, it is difficult to evaluate their performance using only actual MCG or MEG measurements. In this paper, we propose the use of the calibrated MEG phantom for quantitative evaluation of magnetic sensors and present the experimental method. We choose a magneto-impedance (MI) sensor as an example of the magnetic sensor to be evaluated. The magnetic field distribution near the phantom was measured using the MI sensor and a signal source was localized with different averaging numbers and different signal source intensities. The results suggest that the MEG signal cannot be observed in the usual averaging time (i.e., 100), even when the sensor is located near the head; 4.0 mm of source localization accuracy can be achieved with 400-times averaging if the sensor noise decreases to 1/10. The use of the calibrated phantom, instead of examination with human subjects, is effective for quantitative evaluation of the performance of magnetic sensors.

Key words: magnetoencephalography, phantom, magneto-impedance sensor

1. Introduction

Biomagnetic signal measurements, such as magnetoencephalography (MEG) and magneto-cardiography (MCG) are utilized in clinical applications and neuroscience studies. The magnetic signals from the brain and heart are very weak; therefore, superconducting quantum interference device (SQUID) sensors have been used for practical MEG and MCG systems for which the sensitivity is less than 10 fT/Hz$^{1/2}$. On the other hand, SQUID sensors must be cooled by liquid helium to maintain superconductivity. Helium-less MCG or MEG systems are important because of the cost and low availability of liquid helium.

In recent years, the development of refrigerant-less or room-temperature magnetic sensors has advanced, with the aim of realizing new biomagnetic measurement systems. Some groups have succeeded in detecting the magnetic signal from the human heart or brain[1)-6)], and practical applications are expected.

However, the evaluation of such magnetic sensors is difficult with actual MCG or MEG measurement, because there is no guarantee of reproducibility or reliability of the signal sources. Objective evidence is important to prove the effectiveness of newly developed sensors. Additionally, quantitative evaluation is necessary for designing the biomagnetic measurement system using these sensors.

Therefore, the authors propose the use of a phantom for the evaluation of the newly developed magnetic sensors. A phantom is an artificial object that imitates the human body. Quantitative evaluation can be achieved using phantom experiments instead of examination of a human subject. The authors have developed a new phantom and an associated calibration method designed for quantitative evaluation of MEG systems[7)]. This phantom was calibrated and its uncertainty was determined so as to ensure reproducibility and reliability.

In this paper, an evaluation method for a room-temperature magnetic sensor using the calibrated phantom is introduced. As an example of the experimental evaluation with the phantom, we chose a magneto-impedance (MI) sensor that is a candidate for realizing a helium-less MEG system. The experimental setup is detailed in Section 2. The measured data are presented in Section 3. The feasibility of MEG signal detection by the MI sensor is discussed in Section 4.

2. Method

2.1 Phantom

One popular method to analyze the MEG data is to estimate a magnetic source in a human brain using the Sarvas formula[8)]. In the model of the Sarvas formula, the human brain and the source current are a conductive sphere and a current dipole, respectively. There are two types of phantoms: one is the “wet phantom”, composed of two electrodes installed in a sphere filled with saline, and the other is the “dry phantom”, composed of a triangular wire based on Ilmonieimi’s suggestion[9)]. We have chosen the dry-type phantom because it is much easier to handle, maintain, and calibrate.

Figure 1 shows the schematics of the phantom. Two individual isosceles triangles were wound around a quadrangular pyramidal bobbin. The isosceles triangular model has a 5-mm base and 65-mm height. Twenty-five bobbins were assembled inside a domed cover that imitates a human skull. The equivalent current dipoles (ECDs) corresponding to fifty triangular

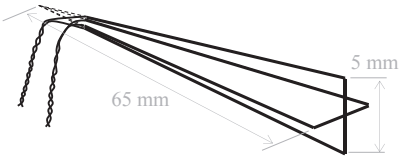

(*a*)

(*b*)

Fig. 1 Configuration of the MEG phantom. (a) schematic of an isosceles-triangular coil pair. (b) photograph of the MEG phantom[7].

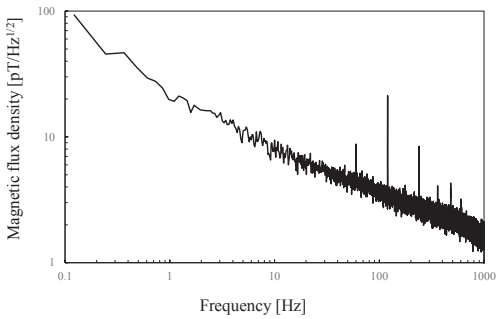

Fig. 2 Noise level of the MI sensor recorded inside a magnetically shielded room.

wires were estimated based on three-dimensional measurement of the current paths and numerical calculations. The details of the phantom configuration and calibration are described in Ref. 7.

2.2 Sensor

In this study, we used a commercially available MI sensor (MI-CB-1DH, Aichi Micro Intelligent Corporation). Figure 2 shows the magnetic noise spectrum recorded inside a magnetically shielded room (MSR). The noise level was approximately 10 pT/Hz$^{1/2}$ at 10 Hz. The noise level of a SQUID sensor for an MEG system should be of femto-Tesla order. Although the sensitivity of the MI sensor is insufficient, the room-temperature sensor has the advantage of being placed at a closer position to the head. Improvement of the signal-to-noise ratio is expected because of the shorter distance between the sensor and the signal source.

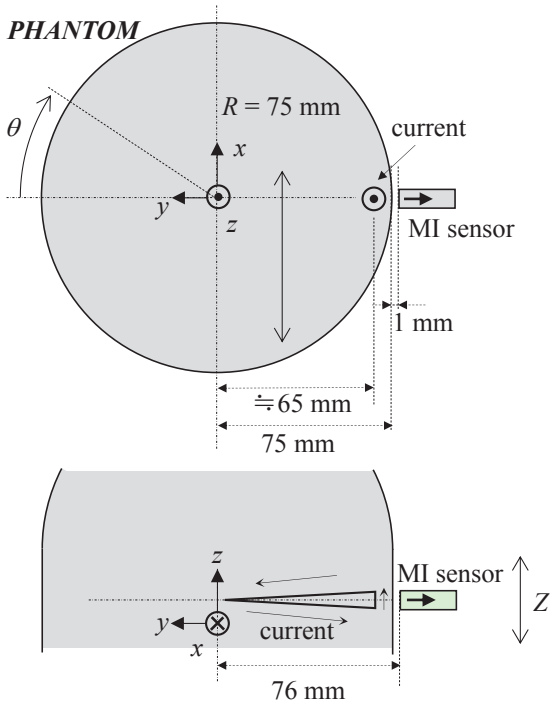

(*a*)

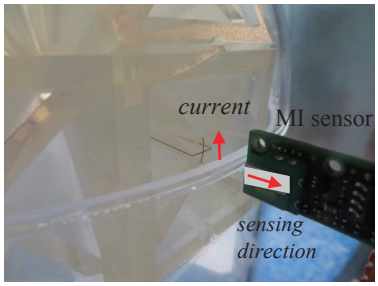

(*b*)

Fig. 3 Setup for experimental evaluation of the MI sensor using the phantom. (a) Schematics of the experimental setup and (b) photograph of the phantom and the MI sensor.

2.3 Experimental setup

Figure 3 shows (a) the experimental setup and (b) the photograph of the phantom and the MI sensor. One triangular wire was chosen for the experiment and an electric current was applied to it by a function generator. The waveform was a sinusoidal burst at a frequency of 11 Hz. The measurement was performed using different current amplitudes I = 10 and 100 μA. The intensity of the ECD corresponding to an applied current amplitude of 10 μA was approximately 50 nA·m. This ECD intensity is similar to that estimated from the recorded data of human auditory evoked responses.

To measure the magnetic field distribution near the phantom, the MI sensor and the phantom were fixed on a three-axial stage and a rotation stage, respectively. The sensing direction of the MI sensor was indicated by arrows in Fig. 3, therefore, the magnetic field normal to the phantom surface was detected by the MI sensor. The total number of measuring points was 54; these

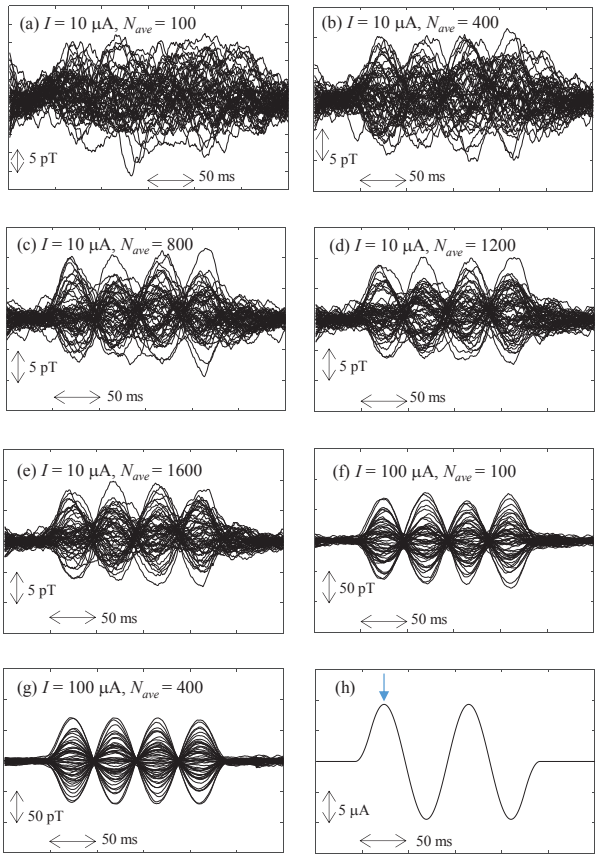

Fig. 4 Measured waveforms (a)-(g) with different current amplitudes (I) and averaging numbers (N_{ave}), and the applied current waveform (h).

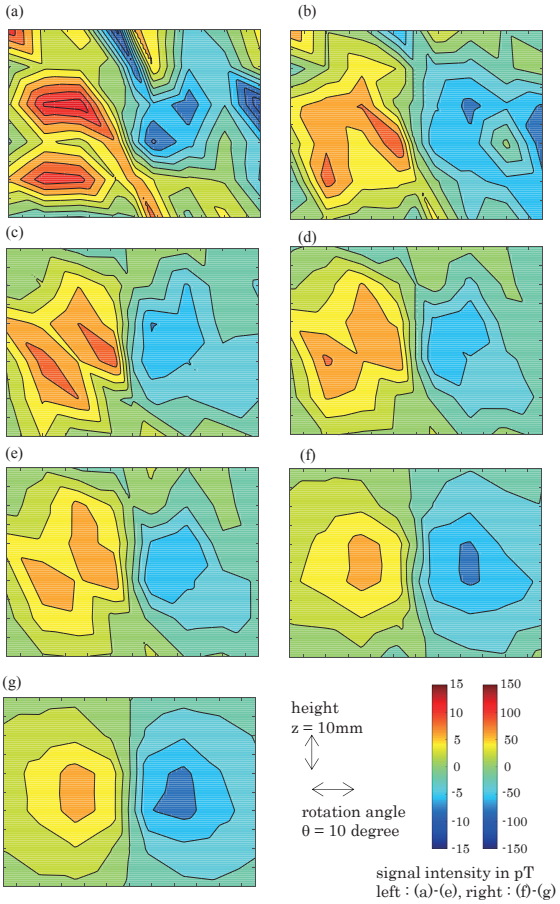

Fig. 5 Contour maps with different current amplitudes (I) and averaging numbers (N_{ave}).

points were obtained by rotating the phantom (θ = 0°, ±4°, ±12°, ±20°, ±28°) and vertically shifting the MI sensor (z = −20, −10, 0, 10, 20, 30 mm). The phantom and the MI sensor were placed in an MSR while measurements were taken.

The output signal of the MI sensor was amplified (×1000) and band-pass filtered (cut-off frequencies = 0.1 Hz and 500 Hz) before recording. The recording was performed by a 16-bit A/D converter (PCIe-6353, National Instruments). The sampling frequency was 2000 Hz, and the recording time was 440 s for I = 10 μA and 120 s for I = 100 μA. After recording, the waveforms were averaged to reduce noise just as in the case we measure a human evoked response. We applied different averaging numbers, namely, 100, 400, 800, 1200, and 1600 for I = 10 μA, and 100 and 400 for I = 100 μA, so as to consider different signal-to-noise ratios. Moving-average processing was also conducted with a window length of 16.5 ms to reduce power-line interference (60 Hz). Then, source localization using the Sarvas formula was conducted for each data set.

3. Result

Figure 4 shows the waveforms of measured data and applied current in (h). The measured waveforms in (a)-(g) correspond to different averaging numbers and applied current amplitude 100, 400, 800, and 1600 for I = 10 μA, and 100 and 400 for I = 100 μA, respectively. The waveform detected at 54 measuring points is overlapped. The applied current waveform when I = 10 μA is shown in Fig. 4 (h).

Figure 5 shows the contour maps of the measured magnetic field distributions. Figure 5 (a) - (g) are the same as those of Fig. 4. The time point of the displayed data was the first peak of the sinusoidal waveform, indicated by a triangular arrow in Fig. 4(h).

The source estimation was conducted using a least-mean-square method and the Sarvas formula. Figure 6 shows the source localization error and goodness-of-fit (GOF) value in the estimation. Figure 6(a)-(g) are the same as those of Figs. 4 and 5. Source estimation was performed at every four peaks of the sinusoidal waveform; the length of the bar indicates the mean value of the source localization error and the GOF. By increasing the signal-to-noise ratio, the source localization error decreased and the GOF increased.

4. Discussion

The amplitude of the magnetic signal from the human brain detected by a SQUID-based MEG system

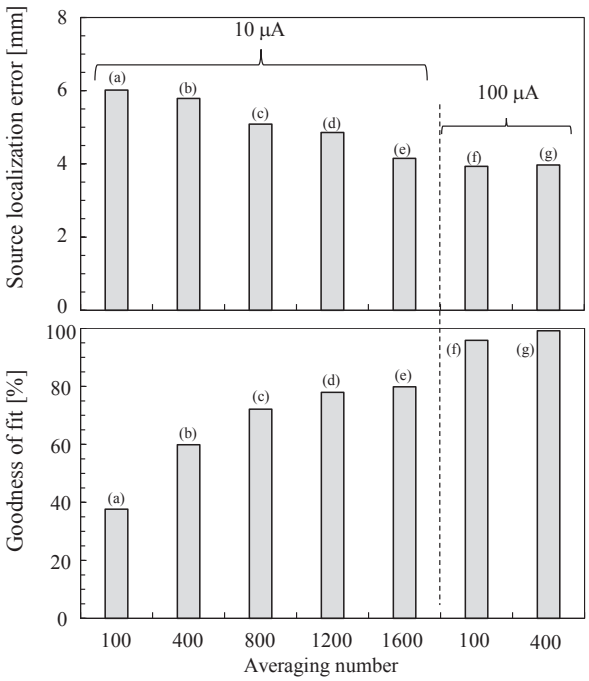

Fig. 6 Source localization error and goodness of fit in ECD analysis.

is typically found to be approximately 1 pT or less. However, larger waveforms, as shown in Fig. 4(e), can be detected by a room-temperature sensor that was located much closer to the target. These results show the possibility of realizing a room-temperature sensor-based MEG system.

When a new magnetic sensor is developed or the sensitivity of a magnetic sensor is improved, the averaging number used to observe the biomagnetic signal is usually considered a criterion for the evaluation of its performance. As shown in Fig. 6, the source localization error with different averaging numbers can be obtained using the phantom. For example, we conclude that 4.2 mm of accuracy and 80% of GOF can be achieved with 1600-times averaging for MEG measurements when using the MI sensor.

In the case of MEG measurement using a SQUID-based system, the averaging number is usually set to approximately 100, in consideration of the trade-off between signal-to-noise ratio and fatigue and/or the duration of concentration of a subject. In contrast, we choose 1600-times averaging as a maximum to obtain a better signal-to-noise ratio. One of the benefits of using the phantom is high reproducibility of the measurement result with a high signal-to-noise ratio based on long-duration measurement.

Furthermore, we also carried out measurements at a current amplitude of 100 μA such that the signal amplitude was 10-times-larger than the human MEG signal. The obtained signal-to-noise ratio is equivalent to that with a 100-times-larger averaging number because the noise decreases in proportion to the square root of the averaging number. Therefore, the results in Fig.6 (f) and (g) correspond to the source localization errors and GOF values at an averaging number of 10000 and 40000 for I = 10 μA, respectively. By applying a large electric current to the phantom, we can obtain a result equivalent to using a large averaging number. From these results, another conclusion is obtained: 4.0 mm of accuracy and over 99% of GOF can be achieved with 400-times averaging if the sensor noise decreases to 1/10. These conclusions provide the target specifications of the room-temperature magnetic sensors used to realize MEG measurements.

In addition, we should point out the value of the source localization error. In this experiment, the smallest source localization error was 4.0 mm when I = 100 μA and the averaging number is 400. This error was much larger than that obtained by the SQUID-based MEG systems[7]. A lower signal-to-noise ratio, smaller measuring points, and a lack of accuracy of sensor positioning are considered to be the causes of the larger source localization error. Specifically, the accuracy of the sensor positioning is supposed to be the major cause of the source localization error because there is a large magnetic field gradient near the signal source comparing with that of SQUID-based MEG systems[10]. It is also important to accurately calibrate the sensor position and orientation to realize the MEG system.

5. Conclusion

We demonstrated the experimental evaluation of the MI sensor using the calibrated MEG phantom. The signal source was estimated from the observed magnetic field distribution at different signal-to-noise ratios. The results showed the possibility (and difficulty) of realizing MEG measurements using the MI sensor. The use of the calibrated phantom is effective for evaluating the performance of magnetic sensors.

Acknowledgements This research was partly supported by The Hokuriku Industrial Advancement Center.

References

1) S. Yabukami, K. Kato, T. Ozawa, N. Kobayashi, and K. I. Arai: *J. Magn. Soc. Jpn.*, **38**, 25 (2014).
2) H. Karo, and I. Sasada: *J. Appl. Phys*, **117**, 17B322 (2015).
3) T. Yamamoto, K. Tashiro, and H. Wakiwaka: *The Papers of Tech. Meeting on "Magnetics"*, MAG-15-9, 41 (2015).
4) H. Xia, A. B-A. Baranga, D. Hoffman, and M. V. Romalis: *Appl. Phys. Lett.*, **89**, 211104 (2006).
5) K. Wang, S. Tajima, Y. Asano, Y. Okuda, N. Hamada, C. Cai, and T. Uchiyama: *Proc. of the 8th Intl. Conf. on Sens. Tech.*, 547 (2014).
6) Y. Ando: *Journal of Japan Biomagnetism and Bioelectromagnetics Society*, **29**, 20 (2016)
7) D. Oyama, Y. Adachi, M. Yumoto, I. Hashimoto, and G. Uehara: *J. Neurosci. Methods*, **251**, 24 (2015).
8) J. Sarvas: *Physics in Medicine and Biology*, **32**, 11 (1987)
9) R. J. Illmonieimi, M. S. Hamalainenm, and J. Knuutila: in

Proc. Biomagnetism: Applications & Theory, New York, Pergamon, 278 (1985)
10) D. Oyama, Y. Adachi, and G. Uehara: *The Papers of Technical Meeting on "Magnetics"*, IEE Japan, MAG-16-1 (2016)

Received Dec. 22, 2016; Revised Mar. 13, 2016; Accepted Apr. 05, 2017

J. Magn. Soc. Jpn., **41**, 75-80 (2017)

<Paper>

Simulation of Extended Source Localization using sLORETA Method for Magnetocardiography

W. Sun and K. Kobayashi

Faculty of Engineering, Iwate University, *4-3-5 Ueda, Morioka, Iwate 020-8551, Japan*

In this study, cardiac source localization was simulated using the spatial filter method. Three types of spatial filters were obtained using the standardized low-resolution brain electromagnetic tomography (sLORETA) method, based on different examination procedures. In Type A filter, the examination was conducted at the front of the torso. In both Type B and Type C filters, the examinations were conducted at the front and back of the torso; however, the distance from the frontal observation plane to the center of the heart model was different for each type. In the simulation experiments, first the goodness of fit (GOF) value was introduced to determine the proper threshold for each spatial filter. Then, single and multiple dipole sources were simulated at different depths with and without noise. The extension of the solutions computed using these spatial filters was investigated. Finally, the performances of these spatial filters, with the corresponding averaged thresholds, were evaluated using the GOF. Type B and Type C spatial filters demonstrated reduction in the extension of source dependency on source depth and improvement in the accuracy of source localization with noisy data.

Key words: Magnetocardiography, sLORETA method, source localization, spatial filter

1. Introduction

Magnetocardiography (MCG) is a noninvasive technique that detects the magnetic field generated by the electrical activity in the heart[1]. Recently, MCG has been attracting a lot of attention in relation to the early detection of heart diseases. As MCG is a multichannel measurement technique and as the signals are not affected by the shape of the lungs and torso[2], it has high potential for clinical applications. MCG aims at obtaining functional mapping, starting from the visualization of signal sources. Because the MCG inverse problem is ill posed and does not have a unique solution, the estimation of MCG signal sources is the biggest challenge for its application[3]. MCG signals are generated by currents flowing within the myocardial fibers during cardiac activity[4]. Therefore, we can consider that an extended source model will be suitable for estimating MCG sources.

The spatial filter methods[5, 6] were developed for MCG source localization, and could be used to obtain a reliable three-dimensional (3D) outline of the heart. Among the many spatial filter methods, standardized low-resolution brain electromagnetic tomography (sLORETA)[7] is widely used for visualizing brain activity, as it has zero localization error for a single dipole with noiseless data. However, it has some limitations, especially under noisy conditions and in case of deep sources[8, 9]. For conventional method, MCG examination is just conducted in the front of the torso, in order to obtain strong signals. In a previous study[10], the spatial filter always favors the sources that are close to the magnetic field sensors and leads to reconstruction of a large extension for deep sources. Namely, the extension of the source depends on the source depth. MCG can detect heart signals not only at the front but also at the back of the torso, even though the signals detected at the back of the torso are very weak[11]. The assessments of the spatial filter based on the different examination method have not been studied. In order to assess the source localization abilities of the spatial filters, and investigate the dependency of source extension on the source depth, the simulation study is needed.

In this study, we make sure the distances from the frontal and back observation planes to the heart are the same, to reduce the dependency of the source extension on the source depth, and obtain a spatial filter that can estimate a cardiac source well with noisy data.

2. Simulation Model

In this study, we simulated MCG source localization using the sLORETA method based on a conventional 64-channel MCG system. Superconducting quantum interference device (SQUID) modules were aligned in an 8 × 8 configuration to create a square observation area sized 175 mm × 175 mm[12].

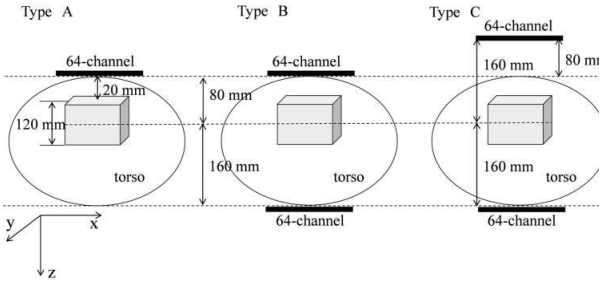

Fig. 1 Frontal and back observation planes and the position of heart in torso.

Simulations were carried out for the 64-channel MCG system within a 168 mm × 168 mm × 120 mm volume. Six thousand six hundred and fifteen voxels were divided with the size of each voxel being 8 mm × 8 mm × 8 mm. Fig. 1 shows three types examination procedures. Type A is the conventional examination method, which is only conducted at the front of the torso. In both Type B and Type C, the examinations are conducted not only at the front but also at the back of the torso; however, the distance from the frontal observation plane to the center of the heart model is different for each type. For Type C, in order to compensate for the varying sensitivities of the sensors to the current sources at different depths, we make sure the distances from the frontal and back observation planes to the heart are the same. The distance from the frontal observation plane to the center of the heart model was set as 80 mm for Type A and Type B and as 160 mm for Type C. The distance from the back observation plane to the center of the heart model was set as 160 mm for Type B and Type C. For the forward problem, we calculated the lead-field matrix $\mathbf{K}$ using the Biot–Savart Law.

3. Methods

sLORETA is a spatial filter method used to solve the ill posed problem. It can obtain a blurred source image by using a linear inverse operator[7].

$$\boldsymbol{\Phi} = \boldsymbol{K}\boldsymbol{J} + \boldsymbol{n} \qquad (1)$$

where $\boldsymbol{\Phi}$ is the detected signals, $\mathbf{K}$ is the lead-field matrix, $\mathbf{J}$ is the original current sources within the heart, and $\mathbf{n}$ is the noise at each sensor. Using the well-known minimum norm estimate (MNE) method, the estimated current sources $\hat{\mathbf{J}}$ can be written as:

$$\hat{\boldsymbol{J}} = \boldsymbol{G}\boldsymbol{\Phi} = \boldsymbol{K}^{\mathrm{T}}\left(\boldsymbol{K}\boldsymbol{K}^{\mathrm{T}} + \lambda^2 \boldsymbol{I}\right)\boldsymbol{\Phi} \qquad (2)$$

where $\mathbf{G}$ is a spatial filter matrix, T denotes the matrix transpose, λ^2 is the Tikhonov regularization parameter, and $\mathbf{I}$ represents an identity matrix. The sLORETA solution can be obtained from the standardization of the MNE solution using its variance in the following way:

$$\hat{\boldsymbol{J}}_{\mathrm{sLORETA},i} = \boldsymbol{S}_{ii}^{-1/2}\hat{\boldsymbol{J}}_i \qquad (3)$$

where $\mathbf{S}_{ii}$ is the diagonal element of the covariance matrix $\mathbf{S}$ with

$$\boldsymbol{S} = \boldsymbol{G}\boldsymbol{K} \qquad (4)$$

In this study, we first calculate the lead-field matrix $\mathbf{K}$ that describes the sensitivity of the sensors to each current source location. For each current source location, $\mathbf{K}$ includes two columns that represent the X component and Y component, respectively. Then, Type A, Type B, and Type C spatial filters are obtained using the sLORETA method.

In the coordinate system, the center point of the top voxels layer is (0, 0, 20) and the unit is mm. A single dipole source (0, 0, 20) in the X direction is simulated by changing the depth in 8 mm increments.

Since the real cardiac sources are considered to be extended sources, simulations with multiple dipoles are also performed. A normal MCG wave is obtained using the Iwate create project 64-channel MCG system[11]. An isomagnetic field map of the MCG wave at the R peak is shown in Fig. 2(a). The generated magnetic field of the multiple sources is shown in Fig. 2(b). Multiple sources—(−16, 8, 20) in the X direction, (−8, 8, 20) in the X direction, and (0, 0, 20) in the Y direction—are simulated by changing the depth in 8 mm increments.

4. Simulation Results and Discussions

4.1 Simulation without Noise

Fig. 3 shows the simulation results of a single dipole at different depths (depth = 28 mm, 76 mm, and 124 mm). The relative strength was normalized by the maximum of the solutions. The white rectangle denotes the maximum of the solutions. All the maximum

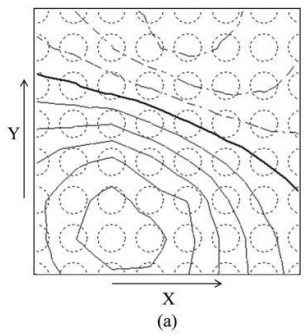

Fig. 2 (a) Isomagnetic field map of MCG wave at R peak. (b) Isomagnetic field map of multiple dipole sources. GOF of two patterns is 0.93. One step of the isomagnetic field contour line is 10 pT.

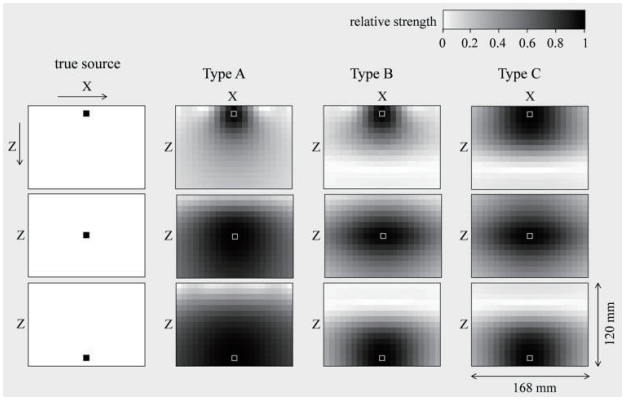

Fig. 3 Left column is the true source in the X direction placed at different depths (from top to bottom depth = 28 mm, 76 mm, and 124 mm). The three right columns are cross sections of simulation results using Type A, Type B, and Type C spatial filters. The white rectangle denotes the maximum of the solutions.

solutions are located at real source positions. It means that there is no localization error without noise. However, the solutions have large spatial extensions. Obviously, the extensions of the solutions computed by the Type A spatial filter have larger dependencies on the depths of the true source than that computed by the Type B and Type C spatial filters. Because a source that is far from the sensor contributes less to the measured data than one that is near the sensor, the solution needs large extensions to fit the measured data. By contrast, Type B and Type C spatial filters produce solutions with extensions that have fewer dependencies on the depths of true sources.

For an extended source, a threshold of relative strength has to be determined. The full width at half maximum (FWHM) is used as the threshold[13, 14]. It means that only the excess 50% of the maximum sources are analyzed to avoid influence from the weak insignificant source estimates. In our study, the goodness of fit (GOF) value is introduced to determine the proper threshold. GOF describes the similarities in the measured and estimated signals at all N sensors[15]. GOF is defined as follows:

$$GOF = 1 - \sum_{i=1}^{N} \left(\boldsymbol{B}_{\mathrm{mea},i} - \boldsymbol{B}_{\mathrm{cal},i} \right)^2 / \sum_{i=1}^{N} \boldsymbol{B}_{\mathrm{cal},i}^2 \qquad (5)$$

where $\boldsymbol{B}_{\mathrm{mea},i}$ denotes the measured magnetic field and

Table 1 Threshold of relative strength simulated with the true source at different depths when the corresponding GOF is close to 1. (All of the GOF is 0.99 in this study).

depth (mm)	Type A	Type B	Type C
20	0.847	0.892	0.940
28	0.830	0.856	0.946
36	0.850	0.860	0.950
44	0.866	0.870	0.940
52	0.902	0.880	0.925
60	0.910	0.883	0.917
68	0.924	0.885	0.911
76	0.934	0.886	0.900
84	0.936	0.910	0.910
92	0.942	0.925	0.920
100	0.942	0.929	0.931
108	0.938	0.938	0.940
116	0.937	0.950	0.952
124	0.927	0.950	0.951
132	0.923	0.947	0.947
average	0.91	0.90	0.93

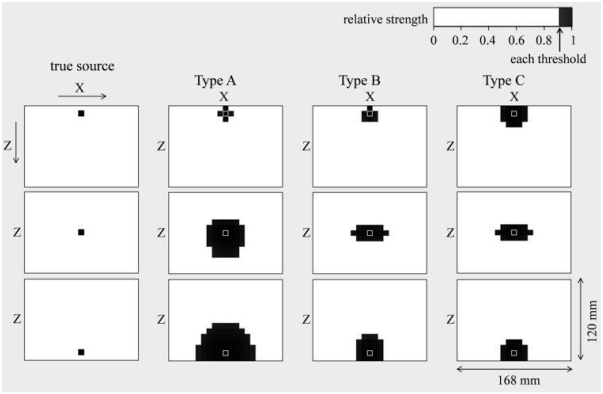

Fig. 4 Left column is the true source in the X direction placed at different depths (from top to bottom depth = 28 mm, 76 mm, and 124 mm). The three right columns are cross sections of simulation results using Type A, Type B, and Type C spatial filters (threshold = 0.91, 0.90, and 0.93, respectively). The white rectangle denotes the maximum of the solutions.

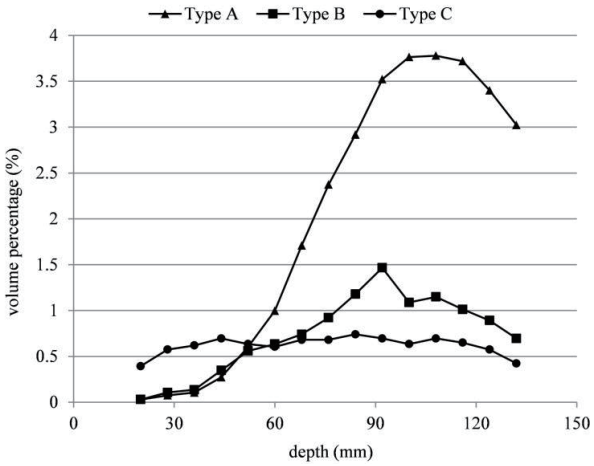

Fig. 5 Relationship of volume percentage and depth of true source.

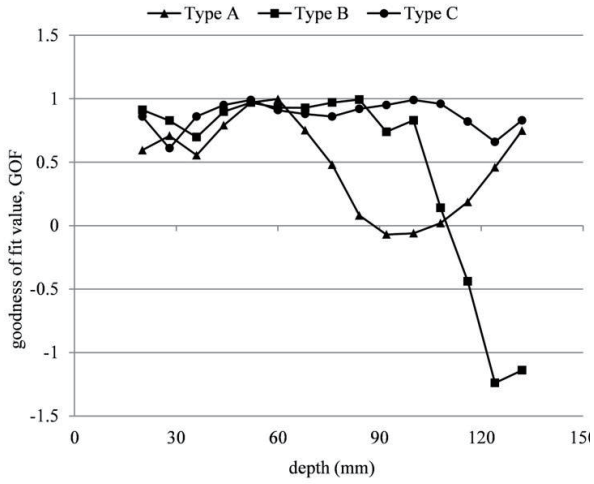

Fig. 6 GOFs of solutions computed using Type A, Type B, and Type C spatial filters when the true source is placed at different depths.

$B_{cal,i}$ denotes the calculated magnetic field at the i^{th} sensor. A high GOF indicates that the estimated sources can explain the measured data well. The threshold values with true sources at different depths are shown in Table 1, when the corresponding GOF is close to 1. The average value is chosen for computing the solutions. The relative strength, which does not exceed the average value of thresholds, is considered to be 0.

In the simulation, a single dipole source in the X direction is placed at different depths (depth = 28 mm, 76 mm, and 124 mm). Fig. 4 shows the cross sections of the solutions computed by Type A, Type B, and Type C spatial filters. The extension of the solution has a large dependency on the depth of the true source for the Type A spatial filter because of the varying solid angles between the dipole at different depths and the observation plane. In addition, the solutions computed by the Type B and Type C spatial filters show smaller extensions in the Z direction than that computed by the Type A spatial filter, owning to the data measured from the back of torso. Because the distances from the frontal and back observation planes to the heart model are the same, the extensions show less dependency on the depth of the true source for the Type C spatial filter.

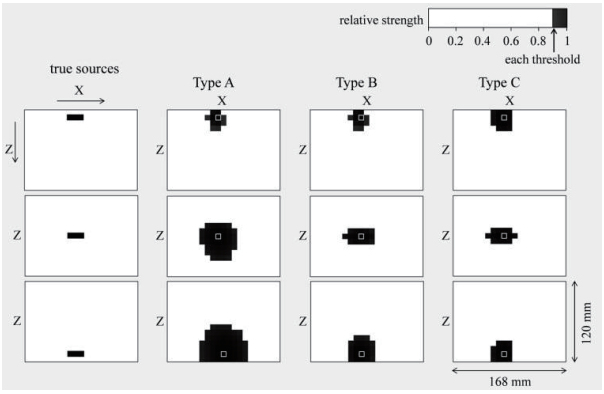

Fig. 7 Left column is the true sources at different depths (from top to bottom depth = 28 mm, 76 mm, and 124 mm). The three right columns are cross sections of simulation results using Type A, Type B, and Type C spatial filters (threshold = 0.91, 0.90, and 0.93, respectively). The white rectangle denotes the maximum of the solutions.

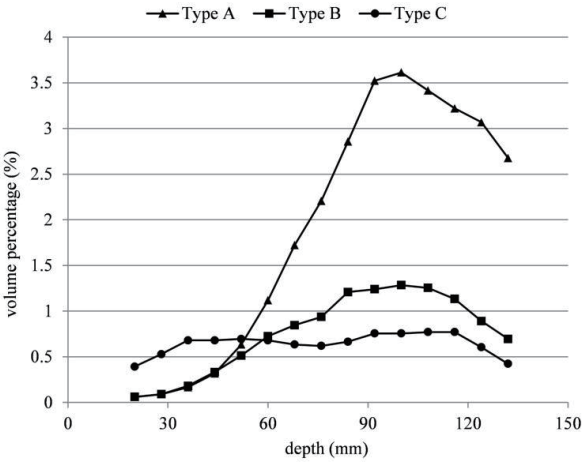

Fig. 8 Relationship of volume percentage and depths of true sources.

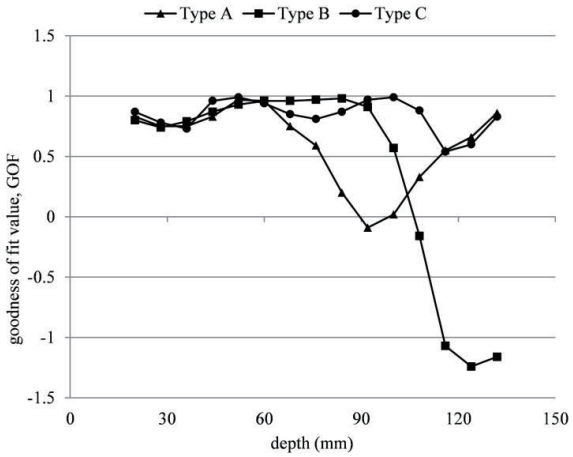

Fig. 9 GOFs of solutions computed using Type A, Type B, and Type C spatial filters when the true sources are placed at different depths.

By computing the volumes of the voxels in which the solutions are localized, the relationship between the volume percentage and the true source depth can be obtained as shown in Fig. 5. The extensions of solutions show less dependency on the depth of the true source for the Type B and Type C spatial filters. The GOFs of Type A, Type B, and Type C spatial filters with the proper thresholds are shown in Fig. 6. The GOF values of the Type A and Type B spatial filters are far away from 1 and even drop to negative values for deep sources. Therefore, the Type C spatial filter shows better performance.

Fig. 7 shows the cross sections of the solutions computed using the Type A, Type B, and Type C spatial filters. By computing the volumes of the voxels in which the solutions are localized, the relationship between the volume percentage and the true source depth can be obtained as shown in Fig. 8. Obviously, the Type B and Type C spatial filters show extensions that have less dependency on the depth of the true sources, compared to the Type A spatial filter. Fig. 9 shows the GOFs of the Type A, Type B, and Type C spatial filters simulated using sources at different depths. The GOFs of Type A and Type B spatial filters are far away from 1 and even drop to negative values for deep sources. It means that these two spatial filters cannot fit the measured data well for deep sources. By contrast, the GOF of the Type C spatial filter has a good performance despite the slight drop in the case of deep sources.

4.2 Simulation with Noisy Data

Since the MCG inverse problem is ill posed, weak noise signals can cause large changes in the solution. In this study, Gaussian white noise is added to the simulated magnetic field data and the inverse solutions

are computed using the above three spatial filters. The SNR ranges from 0 to 40 in 5 dB increments. The SNR is defined as:

$$SNR = 10\log\left\{\mathrm{var}\left(\boldsymbol{B}_{\mathrm{exact}}\right)/\sigma^2\right\} \qquad (6)$$

where $\boldsymbol{B}_{\mathrm{exact}}$ is the variance of the simulated noise-free measurements and σ^2 is the variance of the added Gaussian white noise. In this study, for a single dipole source, the localization error is the distance from the maximum estimated source to the true source. For multiple sources, the localization error is the distance from the maximum estimated source to the center point of the true sources. The mean value is obtained from 100 calculations. In order to obtain the same measurement conditions, the same σ value of noise is set up for these three spatial filters at a certain noise level. Since the magnitudes of the signals detected at the frontal and back observation planes are different, the SNR is different. In this study, the x-axis values of Fig. 10 and Fig. 11 are calculated only using the measurement data that obtained based on Type A examination procedure.

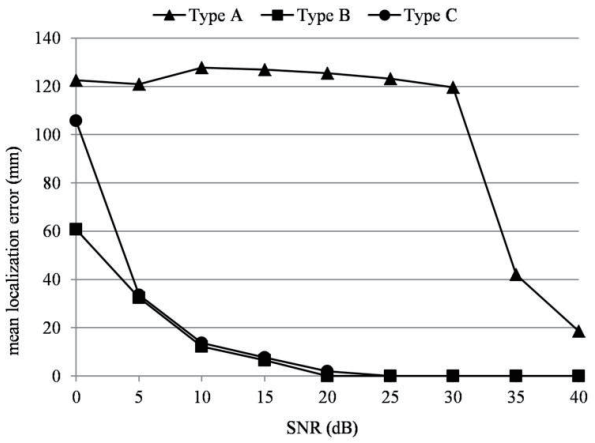

Fig. 10 Mean localization error of single dipole source (depth = 124 mm) with different noise levels.

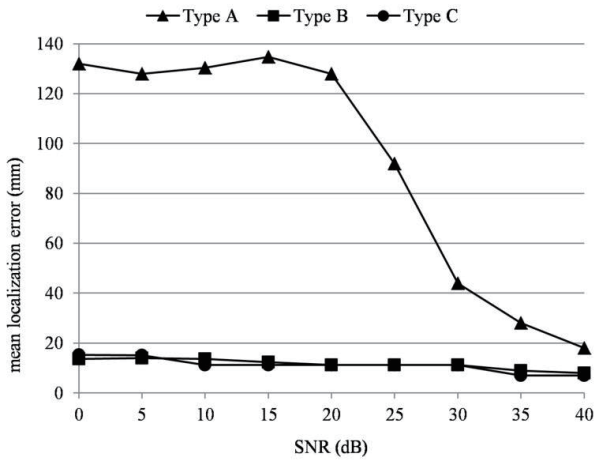

Fig. 11 Mean localization error of multiple sources (depth = 124 mm) with different noise levels.

Fig. 10 and Fig. 11 show the simulation results of a single dipole source and multiple sources, respectively. The single dipole source and the multiple sources are placed at relatively deep positions with a depth of 124 mm. For single dipole source estimation, very weak noise led to Type A spatial filter generating a large localization error. By contrast, the localization errors of Type B and Type C spatial filters were stable and about 0 at 20 ~ 40 dB. For multiple sources estimation, the localization errors of Type B and Type C spatial filters were stable at 0 ~ 40 dB. Apparently, the Type B and Type C spatial filters have improved source localization accuracies. It may be owing to the data obtained from the back of the torso. In addition, Type B and Type C spatial filters have good performances for multiple source localizations even at high noise levels. Hence, they are fit for estimating multiple sources.

5. Conclusion

In this study, Type A, Type B, and Type C spatial filters were obtained using the sLORETA method based on three types of MCG examination procedures. The GOF was introduced to determine the proper threshold for each spatial filter. The extensions of the solutions computed using these spatial filters with the corresponding thresholds were investigated. In the simulation of a single dipole and multiple dipoles placed at different depths, the Type C spatial filter demonstrated an extension that had less dependency on the depth of the true source. In addition, the GOF of the Type C spatial filter was close to 1 even for deep sources. It meant that the Type C spatial filter had the best performance for extended source estimation, compared to Type A and Type B spatial filters. From the results of the simulations with noisy data, we found that the Type B and Type C spatial filters had improved source localization accuracies and that they were fit for estimating extended sources. The reduction of the source extension for deep sources and the improvement of the source localization accuracies owned to the examination at the back of the torso. The same distance from the frontal and back observation planes led to the less dependency of the source extension on the source depth. In the future, we hope to detect the real MCG signals and estimate the cardiac source using Type B and Type C spatial filters.

Acknowledgements This work was supported by the Japan Society for the Promotion of Science KAKENHI (Grants-in-Aid for Scientific Research (C)) Grant Number JP26350535.

References

1) J. S. W. Kwong, B. Leithäuser, J.-W. Park, and C.-M.Yu: *Int. J. Cardiol.*, **167**, 1835 (2013).
2) K. Nakai et al.: *Int. J. Cardiovasc. Imaging*, **21**, 555 (2005).
3) V. Mäntynen, T. Konttila, and M. Stenroos: *Phys. Med. Biol.*, **59**, 7141 (2014).

3) M. De Melis et al.: *J. Magn. Soc. Jpn.*, **34**, 453 (2010).
4) I. Tavarozzi et al.: *Ital. Heart J.*, **3**, 75 (2002).
5) K. Nakai et al.: *Int. J. Cardiovasc. Imaging*, **22**, 573 (2006).
6) G. Shetty and M K: *Int. J. Emerg. Technol. Innov. Res.*, **2**, 1156 (2015).
7) R. D. Pascual-Marqui: *Methods Find. Exp. Clin. Pharmacol.*, **24**,5 (2002).
8) E. Palmero-Soler, K. Dolan, V. Hadamschek and P. A. Tass: *Phys. Med. Biol.*, **52**, 1783 (2007).
9) R. Terusawa et al.: *J. Magn. Soc. Jpn.*, **36**, 272 (2012).
10) M. Yoshizawa, K. Nakai, K. Kobayashi, Y. Nakamura, Y. Uchikawa: *J. Jpn. Biomagn. Bioelectromagn. Soc.*, **15**, 109 (2002).
11) K. Yoshida et al.: *J. Arrhythm.*, **31**, 345 (2015).
12) M. Yoshizawa et al.: *Phys. C: Supercond. Appl.*, **426**, 1572 (2005).
13) F.-H. Lin et al.: *NeuroImage*, **31**, 160 (2006).
14) M. Fuchs, M. Wagner, T. Kohler, and H.-A. Wischmann: *J. Clin. Neurophysiol.* **16**, 267 (1999).
15) K. Pesola et al.: *Med. Biol. Eng. Comput.*, **37**, 2 (1999).

Received Jan. 19, 2017; Accepted May 15, 2017.

Journal of the Magnetics Society of Japan

Vol. 41 No. 4 (通巻第 292 号) 2017 年 7 月 1 日発行

Vol. 41 No. 4 Published Jul 1, 2017
by the Magnetics Society of Japan
Tokyo YWCA building Rm207, 1–8–11 Kanda surugadai, Chiyoda-ku, Tokyo 101–0062
Tel. +81–3–5281–0106 Fax. +81–3–5281–0107

Printed by JP Corporation Co., Ltd.
2–3–36, Minamikase, Saiwai-ku, Kanagawa 212–0055
Advertising agency: Kagaku Gijutsu-sha

発行：（公社）日本磁気学会 101–0062 東京都千代田区神田駿河台 1–8–11 東京YWCA会館 207 号室
製作：ジェイピーコーポレーション 212–0055 神奈川県川崎市幸区南加瀬 2–3–36 Tel.（044）571–5815
広告取扱い：科学技術社 111–0052 東京都台東区柳橋 2–10–8 武田ビル 4F Tel.（03）5809–1132